

LookCloser: Frequency-aware Radiance Field for Tiny-Detail Scene

Xiaoyu Zhang^{1*} Weihong Pan^{2*} Chong Bao² Xiyu Zhang² Xiaojun Xiang¹
 Hanqing Jiang^{1†} Hujun Bao^{2†}
¹SenseTime Research ²State Key Lab of CAD&CG, Zhejiang University



Figure 1. **FA-NeRF** is a frequency-aware framework to capture both the overall scene structure and the high-definition tiny details within a single model, *e.g.*, the clear petal of flowers and sharp texture of wings of the butterfly. Instead, other methods give an over-smooth rendering and lose excessive details. Please see the **Supplementary Video** for an immersive roaming experience.

Abstract

Humans perceive and comprehend their surroundings through information spanning multiple frequencies. In immersive scenes, people naturally scan their environment to grasp its overall structure while examining fine details of objects that capture their attention. However, current NeRF frameworks primarily focus on modeling either high-frequency local views or the broad structure of scenes with low-frequency information, which is limited to balancing both. We introduce **FA-NeRF**, a novel frequency-aware framework for view synthesis that simultaneously captures the overall scene structure and high-definition details within a single NeRF model. To achieve this, we propose a 3D frequency quantification method that analyzes the scene’s frequency distribution, enabling frequency-aware rendering. Our framework incorporates a frequency grid for fast convergence and querying, a frequency-aware feature re-weighting strategy to balance features across different frequency contents. Extensive experiments show that our method significantly outperforms existing approaches

in modeling entire scenes while preserving fine details.

1. Introduction

The Neural Radiance Field (NeRF) has achieved significant success in photo-realistic novel view synthesis and shows great potential for immersive roaming experiences, game and film production, etc. Significant efforts have been invested to enhance the performance of NeRF [1, 15, 33], including improving the high-frequency details [20, 42, 51, 56] of localized scenes or adapting to the expanded scale of scenes [16, 39, 41].

However, in real-world scenarios, both scene structure and intricate details are crucial. Artifacts from incomplete structures or excessive blurring of details can significantly undermine the sense of immersion. To address this, we constructed a dataset—termed the Multi-frequency Dataset—that captures panoramic images for low-frequency structural information and high-resolution images for high-frequency details.

In this work, we aim to provide a high-quality rendering of both scene structures and intricate details across a wide frequency range. However, due to varying view-points and resolutions in the dataset, frequency variations

*Authors contributed equally.

†Corresponding authors.

in the captured 3D signals can differ by the order of magnitude. These extensive frequency variations present substantial challenges for NeRF and its derivatives. While methods such as Mip-NeRF 360 [2] incorporate scale representations by casting cones instead of rays to achieve anti-aliasing and high-quality rendering, they perform unsatisfactorily when reconstructing multi-frequency signals together [9]. This limitation arises from the uniform treatment of pixels, which overlooks the frequency distribution within the scene. Other approaches, such as BungeeNeRF [49] and Strata [9], attempt to address large viewpoint variations by progressively enabling high-frequency feature components to capture fine details, but they struggle to generalize in more varied settings. Adaptive spatial partitioning [34, 46] is another common strategy, designed to selectively capture scene content at different frequencies. However, partitioning based solely on spatial relationships may not align with the actual frequency distribution, potentially limiting the representation of high-frequency details.

To address these challenges, we propose FA-NeRF, a frequency-aware framework for high-fidelity novel view synthesis across broad scene structures and close-up details. FA-NeRF introduces a patch-based 3D frequency quantification method to analyze and embed scene frequency distributions into NeRF’s encoded features, allowing adaptive frequency selection for accurate reconstruction.

Efficiently synthesizing high-quality views with detailed structure remains challenging even with frequency quantification. First, we design a Frequency Grid that stores spatial frequency distributions, enabling rapid convergence and efficient querying. Second, we propose a frequency-aware feature re-weighting strategy to tailor feature frequencies based on scene content, optimizing network capacity. Third, a frequency-averaged sampling strategy adaptively adjusts learning intensity and sampling density for high-frequency content. With the Hash Grid architecture, we maintain a rendering speed of 20 FPS on a single RTX 4090 GPU, even when rendering high-frequency details. In summary, our contributions lie in three aspects:

- The proposed FA-NeRF framework features both the scene’s overall structure and tiny details within a single model, achieving an immersive roaming experience in rendering with large frequency spans.
- A novel patch-based 3D frequency quantification method using image progressive regression and conducting several novel techniques: a frequency grid for fast frequency convergence and query, feature re-weighting, and sampling adjustment to enhance the model’s sensitivity to various frequency content.
- FA-NeRF significantly outperforms the baselines across our Multi-frequency dataset and generalizes well on 2 standard datasets.

2. Related Work

Neural scene representations. The classical work of Mildenhall Ben et al. [29] laid the foundation for the development of NeRF technology, but turns out to be more suitable for reconstructing an object or a bounded small-scale scene due to its huge sampling and Multi-Layer Perception (MLP) access time of training and rendering [10, 23, 28, 32, 35]. Early NeRF works attempted to accelerate the MLP query process by utilizing sparser geometry representation like sparse voxel grid [4, 13, 25, 36, 54], octrees [12, 53], 4D tensor [5, 11, 22, 27] or grid mesh [6, 8, 40, 43, 48], combined with more efficient training and rendering schemes [24, 26, 30, 38]. Instead of using a huge MLP network, Instant-NGP [31] and TensoRF [5] establish a voxel grid to store features followed by a tiny MLP network for efficient training and inference. Recently, 3D Gaussian Splatting (3DGS) [17] and its variants [3, 7, 21, 50, 55, 57] has achieved great success in fast and efficient novel view synthesis by replacing NeRF’s implicit networks with explicit 3D Gaussians and accelerating rendering through differentiable rasterization. However, most of these works are designed to learn a default frequency space without fully considering the frequency distribution within the scene, which limits their ability to effectively capture structures and details in scenarios with significant frequency variations.

Multi-scale Scene Representation. Multi-scale representation [1, 9, 14, 23, 45, 49, 52] propose novel grid-based or anti-aliased representations to preserve multi-scale appearance and details in the trained NeRF model. A typical work is Mip-NeRF [1] which proposes an anti-aliased multi-scale representation by incorporating cone casting and integrated positional encoding (IPE) features into a single multiscale MLP. Mip-NeRF-360 [2] extends Mip-NeRF from object to unbounded scene. Following Mip-NeRF-360 [2] and Instant-NGP [31] reduces the aliasing issue and accelerates the training time by combining a multisampling-like solution with grid-based NeRF model. Some works [9, 49] also focus on training multi-scale scenes by progressively opening high-frequency feature components to learn the details. Although these methods have made effective multi-scale improvements, most of them haven’t learned the explicit 3D distribution of frequencies, which somehow restricts their representation capability for frequency-variant training data.

3. Preliminaries

Neural Radiance Field (NeRF) parameterizes the scene as a continuous implicit function F , mapping a 3D position $\mathbf{x} \in \mathbb{R}^3$ and a viewing direction $\mathbf{d} \in \mathbb{S}^2$ to a color vector $\mathbf{c} \in [0, 1]^3$ and a volumetric density $\sigma \in \mathbb{R}^+$. Each pixel on the image determines a ray emitted from the camera center

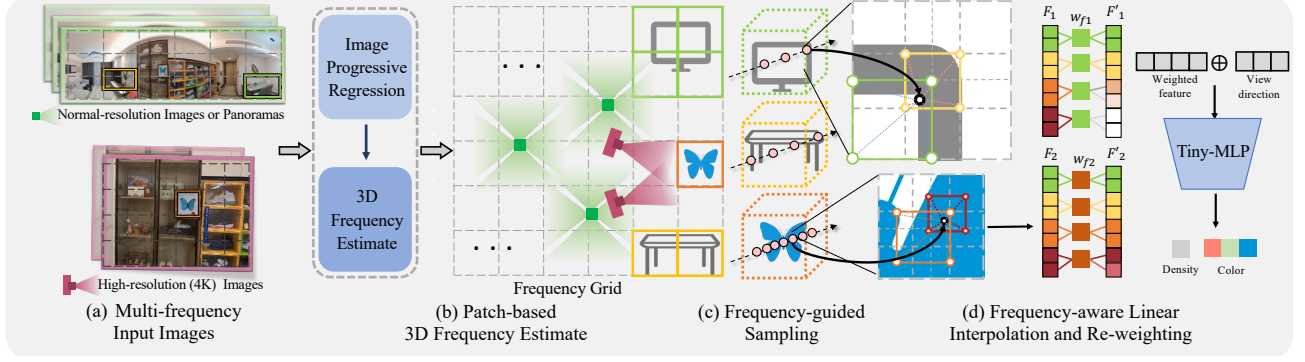


Figure 2. **Overview.** (a) Our input dataset consists of dense normal-resolution images or panoramas of the entire scene structure and high-resolution images focusing on the area of interest of the scene. (b) We propose to quantify the 3D frequency of the scene by progressive image regression and maintain a frequency grid to divide the scene into subspaces with different frequency distributions. (c) We employ a frequency-guided sampling to adaptively control the density of sampling according to the frequency of different objects. (d) Then, the grid-encoded feature of each sample point is re-weighted by the frequency-related weight function. The density and color are decoded by a tiny multilayer perceptron which takes the re-weighted feature and view direction as input.

of projection to the pixel. Instead of sending position \mathbf{x} and direction \mathbf{d} to the network, a positional encoding function is used to map them into a higher dimensional space. This can be formulated as

$$(\mathbf{c}, \sigma) = F_{\theta}(\gamma_{\mathbf{x}}(\mathbf{x}), \gamma_{\mathbf{d}}(\mathbf{d})), \quad (1)$$

where F denotes an MLP with parameters θ , and $\gamma : \mathbb{R}^3 \rightarrow \mathbb{R}^{3(1+2L)}$ a positional encoding function with L frequency channels. The network is then optimized following the volume rendering procedure to represent scenes with photo-realistic rendering.

Frequency components in positional encoding. There are mainly two types of positional encoding. Vanilla NeRF uses Fourier-transformed features to encode the position, and higher Fourier series terms correspond to higher frequency components. NeRF [29] uses a simple concatenation of sines and cosines as a positional encoding function, which is applied to each dimension of the normalized 3D position \mathbf{x} separately:

$$\gamma(\mathbf{x}) = (\sin(2^0 \pi \mathbf{x}), \cos(2^0 \pi \mathbf{x}), \dots, \sin(2^{L-1} \pi \mathbf{x}), \cos(2^{L-1} \pi \mathbf{x})). \quad (2)$$

L determines the highest sampling rate, hence having a critical impact on the fidelity of NeRF.

To remedy the aliasing issue caused by multiscale training data, Mip-NeRF [1] considers a ray as a cone and divides it into several conical frustums whose mean and variance (μ, Σ) are used for integrated position encoding (IPE):

$$\gamma(\mu, \Sigma) = \left\{ \begin{bmatrix} \sin(2^l \mu) \exp(-2^{2l-1} \text{diag}(\Sigma)) \\ \cos(2^l \mu) \exp(-2^{2l-1} \text{diag}(\Sigma)) \end{bmatrix} \right\}_0^{L-1}. \quad (3)$$

In grid-based NeRF, parametric encoding is common. Instant-NGP (iNGP) [31] introduces multi-resolution hash encoding, replacing positional encoding with a pyramid grid that spans coarse to fine resolutions. Each of the L resolution levels in the hash table stores F -dimensional feature vectors at grid corners, and each 3D position \mathbf{x} retrieves a feature vector by interpolating and concatenating features from surrounding corners across levels. The L levels in hash encoding are analogous to frequency channels in frequency encoding: higher resolution levels capture high-frequency components, while lower resolution levels capture low-frequency components.

4. Method

We introduce FA-NeRF, a frequency-aware neural radiance field for high-fidelity novel view synthesis with multi-frequency details (see Fig. 2). Our input images include panoramic shots from a standard camera and high-resolution (up to 4K) images from an SLR camera, with camera poses recovered via structure from motion (SfM). In Sec. 4.1, we estimate the scene’s 3D frequency distribution using a patch-based quantification method. Then, in 4.2, we apply a frequency-aware training framework to preserve these details, utilizing a frequency grid and re-weighting features based on the estimated frequency information.

4.1. Evaluate Frequency Level from 2D to 3D

Inspired by multi-plane image features for novel view synthesis [47], we propose a hypothesis: In the NeRF framework, the geometric or appearance frequency of 3D content can be inferred from the frequency in its degraded 2D image space. To provide a more intuitive description of this process, we created a toy dataset shown in Fig. 3 (a), containing three cubes with the appearance of different-sized

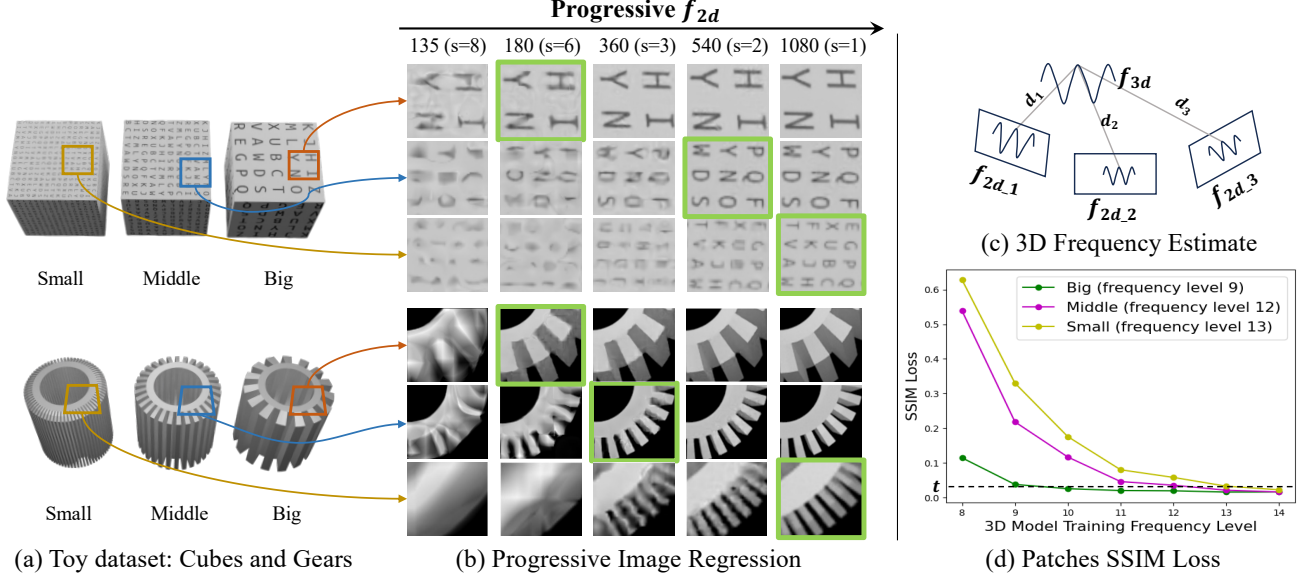


Figure 3. We show 3D frequency quantification on toy examples. (a) The toy datasets comprise three kinds of frequency variations in geometry or texture: three cubes with the appearance of different font sizes, and three gears with the geometry of different pitches. (b) The rendered high-frequency details under different frequencies. "135($s=8$)" means the frequency is 135 and the grid stride s is 8 [31]. The green squares denote the minimal frequency (selected) of the patch for clear reconstruction. (c) The 3D frequency comes from a set of projected 2D frequencies with focal length and depth. (d) The SSIM loss (vertical axis) of training results when using different frequencies (horizontal axis) in three kinds of patches.

letters and three gears with the geometry of different-sized tooth pitches. These two scenes correspond to three different texture frequencies and geometric frequencies respectively.

Progressive image regression. Our key idea is to progressively add higher-frequency encoded feature components of NeRF until the image patch recovers clear structural information. We define this frequency as the 2D frequency of this patch. For a NeRF network in Eq. (1), we use a coordinate-based MLP network to perform image regression: $F_\theta(\mathbf{x}) = \mathbf{c}$, where \mathbf{x} is the 2D coordinate of a sampled pixel and \mathbf{c} is the color. Given a 3D point p and its corresponding patch P , set $\{\hat{P}_{f_1}, \hat{P}_{f_2}, \dots, \hat{P}_{f_n}\}$ represents the rendering results at 2D frequency f_i where i indexes the frequency components and ranges from 1 to n . The target 2D frequency f_{2D} is defined as the minimum frequency f that satisfies $SSIM(P, \hat{P}_f) > t$. SSIM denotes Structural Similarity Index Measure to determine whether the patch fitting meets the required standards, f lies in $\{f_1, f_2, \dots, f_n\}$, and t is a predefined threshold. As depicted in Fig. 3(b), with frequency f increasing from 135 to 1080, the rendering quality gradually improves. The green box indicates the first patch that satisfies the SSIM loss threshold, and the corresponding frequency is the 2D frequency of the 2D image.

3D frequency estimation. For point p and patch P mentioned above, we project the 2D frequency f_{2D} to 3D space with the focal length fl and the depth d of the point to get

its 3D frequency

$$f_{3D}(fl, d) = f_{2D} \cdot \frac{fl}{d}. \quad (4)$$

Since point p has multiple visual patches, its 3D frequency set can be defined as $F = \{f_{3D_j} | j = 1, \dots, m\}$ calculated with patches $\{P_j\}$ and the 3D frequency of point p is defined as the median of set F , as illustrated in Fig. 3(c).

We only perform projection in regions having 2D-3D correspondence because consistency observation is the key to generating coherent 3D content. During the training process, we update the depth with:

$$d(\mathbf{r}) = \int_{t_n}^{t_f} T(t) \cdot \sigma(\mathbf{r}(t)) \cdot t \cdot dt, \quad (5)$$

where t_n and t_f denote the nearest and the farthest distance from the camera center along the ray respectively, and $T(t)$ denotes the accumulated transmittance from t_n to t . In Fig. 3(c), we show the frequency projection process from 2D to 3D space.

Moreover, as depicted in Fig. 3(d), green, magenta, and yellow lines represent patches with 3D frequency levels of 9, 12, and 13, respectively. As the training frequency level increases from 8 to 14, the SSIM loss of rendered patches gradually decreases. When the training frequency reaches the corresponding 3D frequency of each patch, the SSIM loss drops below the threshold. This indicates that: 1) The

minimum NeRF frequency level required to fully restore the structures and the textures of different 3D frequencies in the scene varies; 2) Our 3D frequency estimation for the 3D contents accurately reflects their true frequencies.

This conclusion is helpful for understanding rendering performance in multi-frequency scenes.

4.2. Frequency-aware Framework

Directly training on multi-level frequency data may lead to incorrect geometry and make convergence difficult [9, 49]. "Coarse-to-fine" is a widely adopted learning strategy [12, 37, 44], which first reconstructs the scene structure using low-frequency feature components and then promotes detail recovery using high-frequency feature components. However, in complex multi-frequency data, these strategies cannot accurately restore details without knowing the frequency hierarchy of the target objects. Moreover, as shown in Fig. 4 (a), the sampling strategy affects the rendering results in different frequency surfaces. Therefore, we propose a frequency grid to store the frequency distribution of the scene and adjust the NeRF-encoded features at different frequency levels through re-weighting to make more efficient use of NeRF-encoded feature space for various frequency content and adjust the sampling strategy to enhance learning high-frequency content.

Frequency grid. We use a frequency voxel grid $\mathbf{V}^{(\text{frequency})} \in \mathbb{R}^{N_x \times N_y \times N_z \times 1}$ to store spatial occupancy information and records the frequency information of the content occupying the space, as illustrated in Fig. 2(b). $\mathbf{V}^{(\text{frequency})}$ is initialized by the point cloud. Given a 3D point p in the point cloud and its observation images, we re-project it to these images and set $\{P_i | i = 1, \dots, n\}$ denotes n corresponding patches where the re-projected point locates. n equals the number of observation images of point p . As mentioned in Section 4.1, each point p has its 3D frequency f_{3D} . Thus the $\mathbf{V}^{(\text{frequency})}$ is initialized with $f_{grid} = \max \{f_{3D_j} | j = 1, \dots, m\}$ where m denotes the amount of 3D points in this grid. The values stored in the $\mathbf{V}^{(\text{frequency})}$ are normalized according to the scale of the scene to ensure consistency with the encoded feature frequency components of NeRF.

As we gradually reconstruct the scene structure and get the depth of the training ray, the frequency value is updated using Eq. (4). Since all the 2D frequencies f_{2D} have been obtained, this process consumes only a negligible amount of computational resources.

Frequency re-weighting. To achieve a better balance of features across varying frequencies, we re-weight the feature at each frequency level based on the quantified frequency in $\mathbf{V}^{(\text{frequency})}$. Although high-frequency feature components contribute little to low-frequency content, directly decomposing features to separately learn multi-frequency content is not effective [49]. Therefore, by ap-

plying smooth re-weighting, we adjust the sensitivity of each frequency component in the NeRF-encoded features, thereby preventing wasting the expressive capacity of high-frequency feature components on low-frequency content. In Instant-NGP [31], the sampled point, whose spatial location is \mathbf{x} , will be first scaled by the grid linear size n_ℓ at the frequency (*i.e.* level) ℓ . The feature of the sampled point at the frequency ℓ comes from tri-linear interpolation within hash grid V_ℓ . These vectors are directly concatenated to form the encoded feature \mathbf{f} . However, we do not directly concatenate these vectors; instead, we apply a frequency-related down-weighting factor:

$$\omega_\ell = \text{erf}\left(\sqrt{\frac{(\ell_{\max} - \ell_{\min})^2}{\text{Clip}[(\ell_{\max} - \ell + 1)^2, \{1, (\ell_{\max} - \ell_{\min})^2\}]}}\right), \quad (6)$$

where ℓ_{\min} and ℓ_{\max} are the minimum and maximum frequency in $\mathbf{V}^{(\text{frequency})}$ respectively, and $\omega_\ell \in [0, 1]$, before that:

$$\mathbf{f} = \text{concat}_{\ell=0..k}(\omega_\ell \cdot \text{trilerp}(n_\ell \cdot \mathbf{x}; V_\ell)), \quad (7)$$

where k is the number of levels in the hash grid V . Since low-frequency feature components are used in learning high-frequency content, we opt for a one-sided weight reduction function.

Frequency-averaged sampling. Since the complexity of geometry or texture in the high-frequency area is more than that of the low-frequency area, the high-frequency area deserves more extensive learning. However, random pixel sampling within the dataset uses a uniform probability for low-frequency and high-frequency areas in a training batch. Therefore, we propose a frequency-averaged sampling (FAS) strategy. Assume there are N effective frequencies in the scene and each frequency contains a patch set of size $n(n > 0)$. We evenly divide a training batch into N segments. Each segment samples pixels within a corresponding frequency patch, thereby increasing the sampling probability of high-frequency areas. To achieve a high-quality novel view synthesis, we don't sample the entire patch; instead, we adjust the probability of pixels being sampled on a patch-by-patch basis. We progressively employ this sampling strategy to encourage the network to form the correct geometry first. For more details, please refer to the supplementary material.

Adaptive Ray Marching. The sampling interval in ray marching affects the quality of high-frequency details, especially when reconstructing high-frequency details at the scale of the entire scene. Recall that NeRF models a 3D scene using a rendering function as Eq. 1, which maps the coordinates of a 3D point to the properties of the scene.

The ray sampling interval refers to the distance between adjacent sample points along a ray. As shown in Fig. 4(a),

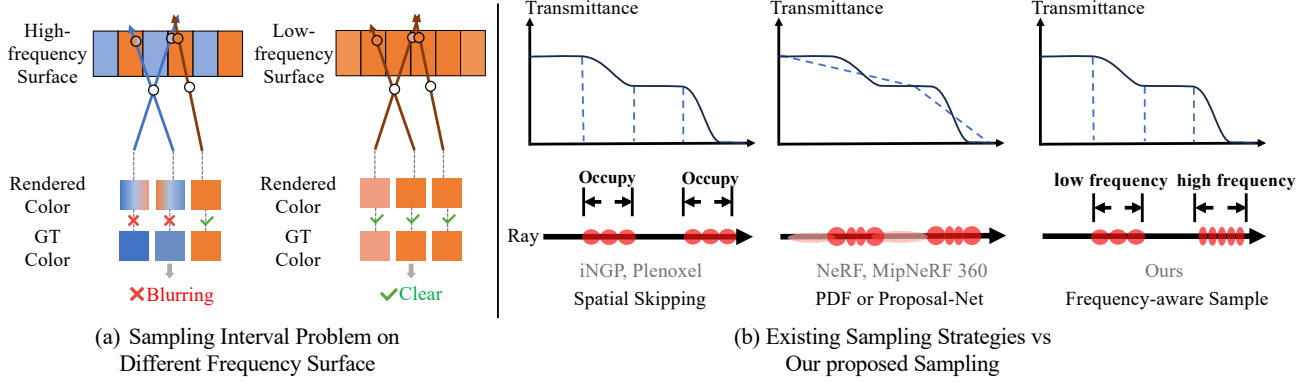


Figure 4. (a) We illustrate the sampling interval problem on different frequency surfaces. While using larger sampling intervals still achieves correct results on the low-frequency surface, it leads to misleading results on the high-frequency surface, resulting in excessive smoothing. (b) We compare three sampling strategies along the ray. Our strategy adjusts the sampling interval to match the content’s frequency.

with a large sampling interval, the low-frequency surfaces can recover their original colors, while high-frequency areas are prone to rendering incorrect colors due to the sampling points too far from the surface, resulting in blurred outcomes. When the sampling interval is reduced, the sampling points in the high-frequency areas are closer to the surface, thus generating more accurate results.

Therefore, many studies adjust the sampling interval by manually tuning the sampling steps or setting different proposal steps for different scenes to achieve optimal performance. We adjust the sampling interval based on the quantified frequency grid to accommodate the sampling needs of high-frequency areas. The common sampling methods are compared in the Fig. 4(b). Spatial skipping based on the occupancy grid is the degraded form of our sampling method. Given the frequency value f of the frequency grid traversed by ray I , the sampling frequency f_{sample} should be ensured to be less than twice the detail frequency to comply with the sampling theorem, *i.e.* the sampling frequency is $f_{sample} = 2f$. Based on this formula, we can estimate an appropriate sampling interval according to the frequency of the content, eliminating the need to tune the sampling hyperparameters for different scenes.

Training Loss: The training loss is defined as

$$\mathcal{L}_{total} = \mathcal{L}_{recon}(\hat{\mathbf{c}}, \mathbf{c}_{gt}) + \quad (8)$$

$$\lambda_{dist} \mathcal{L}_{dist}(\mathbf{s}_d, \mathbf{w}) + \lambda_{depth} \mathcal{L}_{depth}, \quad (9)$$

where $\mathcal{L}_{recon}(\hat{\mathbf{c}}, \mathbf{c}_{gt}) = \sqrt{(\hat{\mathbf{c}} - \mathbf{c}_{gt})^2 + \epsilon}$ is a color reconstruction loss, $\hat{\mathbf{c}}$ is the rendered pixel color, \mathbf{c}_{gt} is the ground-truth pixel color, $\epsilon = 10^{-4}$. We regularize the density distribution in disparity through \mathcal{L}_{dist} , which is proposed by Mip-NeRF360 [2], where \mathbf{s}_d is the set of normalized ray distances and \mathbf{w} is the set of weights. It penalizes the discreteness to encourage the formation of thinner surfaces. In contrast to Mip-NeRF 360 using a proposal net-

work to obtain sampling suggestions, we compute this discrete version of sampling distribution regularization along the entire ray. \mathcal{L}_{depth} is the depth loss between the estimated depth and the actual value from the sparse point cloud, which is used in early training to avoid incorrect geometry formation. λ_{dist} , λ_{depth} are the coefficients of loss. We provide more training details in the supplementary material.

5. Experiments

5.1. Experimental Settings

Datasets. We use two kinds of datasets for evaluation. (1) Multi-frequency dataset with a large frequency span. The Multi-frequency dataset contains five indoor scenes, each of them contains dense normal-resolution (less than 2K) images for the entire structure of the scene and high-resolution (up to 4K) images focusing on the area of interest of the scene; (2) Standard dataset with a small frequency span. The dataset contains five bounded scenes from the MipNeRF-360 dataset [2] and two unbounded scenes from the Tanks&Temples dataset [19]. For all datasets, we use the standard settings that select one out of every eight images as the testing set, and the remaining images as the training set. PNSR, SSIM, and LPIPS_(VGG) are employed as evaluation metrics.

Baselines and Implementation. 3D-GS [17], MipNeRF-360 [2] and Instant-NGP [31] and TensorRF [5] are selected as our baselines. We set a constant batch size of 2^{18} for point samples. Ray batch sizes vary based on the average number of sampled points per ray. We employ the Adam optimizer [18] for parameter training with $\beta_1 = 0.9$, $\beta_2 = 0.99$, $\epsilon = 10^{-15}$. For the Multi-frequency dataset, we train all methods for 200k steps to achieve full convergence. For MipNeRF-360 and Tanks & Temples dataset, our method

Table 1. **Quantitative comparisons on the MULTI-FREQUENCY DATASET dataset.** The **best**, **second best**, and **third best** results are highlighted in red, orange, and yellow, respectively.

Method—Metric	Structure View (600×600)			Detail View (4032×3024)		
	PSNR \uparrow	SSIM \uparrow	LPIPS $\downarrow_{(VGG)}$	PSNR \uparrow	SSIM \uparrow	LPIPS $\downarrow_{(VGG)}$
TensoRF	28.88	0.854	0.256	22.76	0.781	0.430
iNGP-Base	30.27	0.893	0.216	23.63	0.784	0.408
iNGP-Big	30.97	0.909	0.183	24.00	0.786	0.398
Mip-NeRF360	30.79	0.906	0.188	24.16	0.792	0.383
3D-GS	30.85	0.897	0.191	24.29	0.802	0.390
Ours	32.44	0.929	0.148	26.29	0.843	0.332

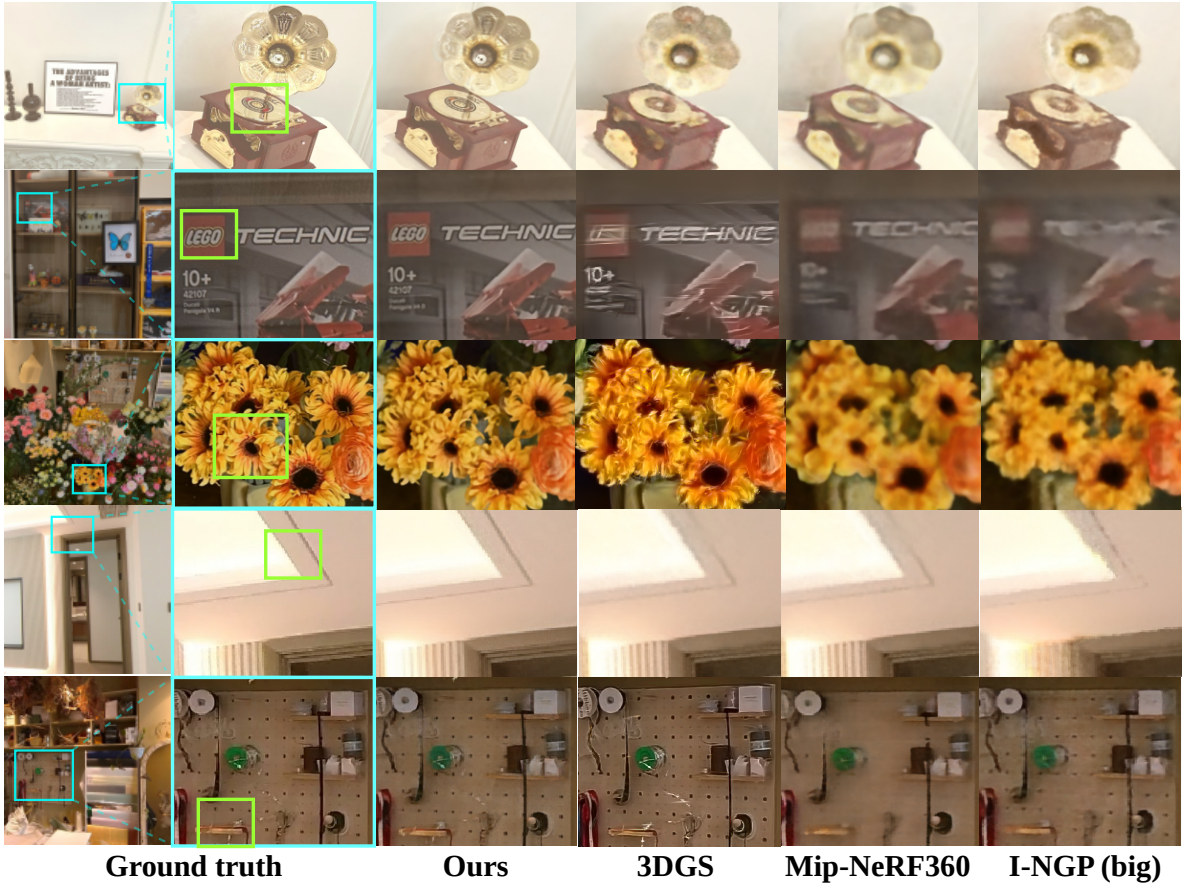


Figure 5. **Qualitative comparison.** We show the qualitative comparison results with 3D-GS [17], Mip-NeRF360 [2], and Instant-NGP [31] on the MULTI-FREQUENCY DATASET. NeRFs tend to produce overly blurred results on high-frequency data, while 3D-GS often exhibits noticeable spiky artifacts. In contrast, our method faithfully preserves high-frequency details and geometric structures in scenes with large frequency variations.

and Instant-NGP are trained for 50k steps with the same batch size. For all datasets, we report results for a basic configuration of Instant-NGP (base) as well as a slightly larger hash table size (Big). All the methods are trained on a single RTX 4090 GPU.

5.2. Results Analysis

In Tab. 14, we report the quantitative evaluation results on the Multi-frequency dataset. Our method significantly surpasses all benchmark methods, both for normal-resolution images and high-resolution images. Our method does not only reconstruct the intact low-frequency structure of the

scene, *e.g.*, the clear ceiling in *Home* and complete circuit board in *Flower Shop*, but also recover sharp high-frequency contents, *e.g.*, well-preserved of details of the phonograph in *Music Room*, clear text of the lego in *Home*, and vivid appearance of the flower in *Flower Shop*. Unlike the excessive blurring produced by NeRF-based methods, 3D-GS introduces numerous needle-like artifacts under large frequency spans. While it exhibits a sharp appearance, it fails to accurately capture the true details of the scene. TensoRF[5] has the lowest PSNR metric due to its compression of high-frequency spatial information and is not included in the qualitative comparison. The results of Mip-NeRF 360 [2] are blurry in both low-frequency and high-frequency images because the continuity of MLP over-smooth significant frequency changes. The results of iNGP-Big appear sharper with more content, but due to the uniform partitioning of space and sampling, it lack clarity. This demonstrates that simply increasing capacity is insufficient to model multi-frequency content. In contrast, our method can capture various frequencies within the scene through its frequency-aware design, thus enabling better restoration of both low-frequency structures and high-frequency details in multi-frequency contents.

5.3. Ablation Studies

Frequency Issues in Standard Datasets. We evaluate our method on MipNeRF-360 [2] and Tanks & Temples [19], both object-centric datasets, and still demonstrates improvements. This indicates that multi-frequency issues exist in general datasets, as images with the same resolution can capture different frequency content. Since these datasets have a smaller frequency span than our Multi-frequency dataset, it does not significantly degrade rendering quality. Nevertheless, our multi-frequency optimization still benefits the high-fidelity modeling of various frequency components in the scene.

Component Ablation. We conduct ablation studies in the *Music Room* of the Multi-frequency dataset. In the ablation studies, we individually deactivate the frequency-aware components, namely feature re-weighting, frequency-averaged sampling (FAS), and Adaptive Ray Marching (ARM), to test their effectiveness. Furthermore, we test the rendering results without our Frequency Grid by setting the frequency to a uniform value, thus disabling all the components mentioned above.

As shown in Tab. 15, model (A) without the Frequency Grid performs worst, further confirming the effectiveness of our Frequency Grid in multi-frequency scenarios. Among all the frequency-aware components, disabling ARM causes the most significant performance drop. This is because high-frequency contents require denser sampling in the scene with a large frequency span, as described in Sec. 4.2. Disabling frequency-averaged sam-

Table 2. Quantitative comparisons on the MipNeRF-360 [2] dataset and Tanks&Temples [19] dataset.

Dataset	MipNeRF-360			Tanks&Temples		
Method—Metric	PSNR [†]	SSIM [†]	LPIPS _(VGG) [†]	PSNR [†]	SSIM [†]	LPIPS _(VGG) [†]
TensoRF	24.71	0.708	0.448	19.52	0.613	0.451
iNGP-Base	29.15	0.879	0.216	21.56	0.731	0.318
iNGP-Big	29.72	0.900	0.219	21.69	0.757	0.280
Mip-NeRF360	31.49	0.916	0.179	22.22	0.759	0.257
3D-GS	30.95	0.926	0.167	24.36	0.831	0.213
Ours	31.20	0.931	0.165	24.45	0.821	0.205

Table 3. Ablation Results for Different Components

Setting	normal-res(600×600)			high-res(4032×3024)		
	PSNR [†]	SSIM [†]	LPIPS _(VGG) [†]	PSNR [†]	SSIM [†]	LPIPS _(VGG) [†]
A) w/o Frequency Grid	31.95	0.930	0.181	24.90	0.910	0.316
B) w/o Feature Re-weighting	33.58	0.932	0.167	26.73	0.923	0.256
C) w/o FAS	33.50	0.929	0.163	25.84	0.921	0.268
D) w/o adaptive RM	32.30	0.928	0.165	25.42	0.922	0.255
E) Our Complete Model	33.52	0.931	0.162	26.97	0.924	0.250

pling reduces training frequency, hindering high-resolution rendering performance. Additionally, turning off feature re-weighting degrades high-resolution performance but improves normal-resolution results. This suggests that in multi-frequency scenarios, low-frequency signals overshadow high-frequency ones, causing performance drops, especially when feature space capacity is limited, such as with a smaller hash table.

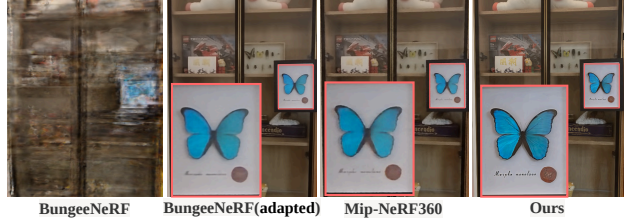


Figure 6. Additional comparisons with BungeeNeRF

Additional comparison with Multi-Scale Method. We also compared BungeeNeRF due to its ability in cross-scale rendering. This divide-and-conquer strategy is commonly used in Multi-Scale and Large-Scale tasks, but in real scenes, the frequency distribution isn't strictly based on position. To make a fair comparison, we modified BungeeNeRF by assigning high-resolution cameras to the "close views" block and increasing the position encoding frequency to (2^{11}) . Qualitative results in Fig.6 show that BungeeNeRF performs similarly to its baseline (Mip-NeRF) in multi-frequency scenarios. Quantitative results are in the supplementary.

6. Conclusion

Our experiments demonstrate that we can effectively quantify the frequency components within a scene and perform targeted high-fidelity reconstruction. This is crucial for reconstructing scenes with tiny details. Our method outperforms all state-of-the-art approaches, and given the immersive effects, such scenes may inspire future research. While our grid-based representation enables 20 FPS rendering, there is still potential for further acceleration.

References

- [1] Jonathan T Barron, Ben Mildenhall, Matthew Tancik, Peter Hedman, Ricardo Martin-Brualla, and Pratul P Srinivasan. Mip-NeRF: A multiscale representation for anti-aliasing neural radiance fields. In *Proceedings of the IEEE/CVF International Conference on Computer Vision*, pages 5855–5864, 2021. 1, 2, 3
- [2] Jonathan T Barron, Ben Mildenhall, Dor Verbin, Pratul P Srinivasan, and Peter Hedman. Mip-NeRF 360: Unbounded anti-aliased neural radiance fields. In *Proceedings of the IEEE/CVF Conference on Computer Vision and Pattern Recognition*, pages 5470–5479, 2022. 2, 6, 7, 8, 3
- [3] Samuel Rota Bulò, Lorenzo Porzi, and Peter Kotschieder. Revising densification in gaussian splatting, 2024. 2
- [4] Anpei Chen, Zexiang Xu, Andreas Geiger, Jingyi Yu, and Hao Su. Tensorf: Tensorial radiance fields. In *ECCV*, 2022. 2
- [5] Anpei Chen, Zexiang Xu, Andreas Geiger, Jingyi Yu, and Hao Su. Tensorf: Tensorial radiance fields. In *European Conference on Computer Vision*, pages 333–350. Springer, 2022. 2, 6, 8
- [6] Zhiqin Chen, Thomas Funkhouser, Peter Hedman, and Andrea Tagliasacchi. MobileNeRF: Exploiting the polygon rasterization pipeline for efficient neural field rendering on mobile architectures. In *Proceedings of the IEEE/CVF Conference on Computer Vision and Pattern Recognition*, pages 16569–16578, 2023. 2
- [7] Kai Cheng, Xiaoxiao Long, Kaizhi Yang, Yao Yao, Wei Yin, Yuexin Ma, Wenping Wang, and Xuejin Chen. Gaussianpro: 3d gaussian splatting with progressive propagation, 2024. 2
- [8] Paul E. Debevec, Camillo J. Taylor, and Jitendra Malik. Modeling and rendering architecture from photographs: A hybrid geometry- and image-based approach. In *SIG-GRAPH*, 1996. 2
- [9] Ankit Dhiman, R Srinath, Harsh Rangwani, Rishabh Parihar, Lokesh R Boregowda, Srinath Sridhar, and R Venkatesh Babu. Strata-NeRF: Neural radiance fields for stratified scenes. In *Proceedings of the IEEE/CVF International Conference on Computer Vision*, pages 17603–17614, 2023. 2, 5
- [10] Rizal Fathony, Anit Kumar Sahu, Devin Willmott, and J Zico Kolter. Multiplicative filter networks. In *International Conference on Learning Representations*, 2020. 2
- [11] John Flynn, Michael Broxton, Paul E. Debevec, Matthew DuVall, Graham Fyffe, Ryan S. Overbeck, Noah Snavely, and Richard Tucker. Deepview: View synthesis with learned gradient descent. In *CVPR*, 2019. 2
- [12] Sara Fridovich-Keil, Alex Yu, Matthew Tancik, Qinhong Chen, Benjamin Recht, and Angjoo Kanazawa. Plenoxels: Radiance fields without neural networks. In *Proceedings of the IEEE/CVF Conference on Computer Vision and Pattern Recognition*, pages 5501–5510, 2022. 2, 5
- [13] Peter Hedman, Pratul P Srinivasan, Ben Mildenhall, Jonathan T Barron, and Paul Debevec. Baking neural radiance fields for real-time view synthesis. In *Proceedings of the IEEE/CVF International Conference on Computer Vision*, pages 5875–5884, 2021. 2
- [14] Wenbo Hu, Yuling Wang, Lin Ma, Bangbang Yang, Lin Gao, Xiao Liu, and Yuewen Ma. Tri-MipRF: Tri-Mip representation for efficient anti-aliasing neural radiance fields. In *Proceedings of the IEEE/CVF International Conference on Computer Vision*, pages 19774–19783, 2023. 2
- [15] Xin Huang, Qi Zhang, Ying Feng, Xiaoyu Li, Xuan Wang, and Qing Wang. Local implicit ray function for generalizable radiance field representation. In *Proceedings of the IEEE/CVF Conference on Computer Vision and Pattern Recognition*, pages 97–107, 2023. 1
- [16] Brian K. S. Isaac-Medina, Chris G. Willcocks, and Toby P. Breckon. Exact-nerf: An exploration of a precise volumetric parameterization for neural radiance fields. In *Proceedings of the IEEE/CVF Conference on Computer Vision and Pattern Recognition (CVPR)*, pages 66–75, 2023. 1
- [17] Bernhard Kerbl, Georgios Kopanas, Thomas Leimkühler, and George Drettakis. 3d gaussian splatting for real-time radiance field rendering. *ACM Trans. Graph.*, 42(4):139–1, 2023. 2, 6, 7
- [18] Diederik P Kingma and Jimmy Ba. Adam: A method for stochastic optimization. *arXiv preprint arXiv:1412.6980*, 2014. 6
- [19] Arno Knapitsch, Jaesik Park, Qian-Yi Zhou, and Vladlen Koltun. Tanks and temples: Benchmarking large-scale scene reconstruction. *ACM Transactions on Graphics*, 36(4), 2017. 6, 8, 3
- [20] Qewei Li, Feichao Li, Jie Guo, and Yanwen Guo. Uhdnerf: Ultra-high-definition neural radiance fields. In *Proceedings of the IEEE/CVF International Conference on Computer Vision (ICCV)*, pages 23097–23108, 2023. 1
- [21] Yanyan Li, Chenyu Lyu, Yan Di, Guangyao Zhai, Gim Hee Lee, and Federico Tombari. Geogaussian: Geometry-aware gaussian splatting for scene rendering, 2024. 2
- [22] Zhengqi Li, Wenqi Xian, Abe Davis, and Noah Snavely. Crowdsampling the plenoptic function. In *ECCV*, 2020. 2
- [23] David B Lindell, Dave Van Veen, Jeong Joon Park, and Gordon Wetzstein. Bacon: Band-limited coordinate networks for multiscale scene representation. In *Proceedings of the IEEE/CVF Conference on Computer Vision and Pattern Recognition*, pages 16252–16262, 2022. 2
- [24] Lingjie Liu, Jiatao Gu, Kyaw Zaw Lin, Tat-Seng Chua, and Christian Theobalt. Neural sparse voxel fields. In *NeurIPS*, 2020. 2
- [25] Lingjie Liu, Jiatao Gu, Kyaw Zaw Lin, Tat-Seng Chua, and Christian Theobalt. Neural sparse voxel fields. *Advances in Neural Information Processing Systems*, 33:15651–15663, 2020. 2
- [26] Julien NP Martel, David B Lindell, Connor Z Lin, Eric R Chan, Marco Monteiro, and Gordon Wetzstein. Acorn: Adaptive coordinate networks for neural scene representation. *arXiv preprint arXiv:2105.02788*, 2021. 2
- [27] Ben Mildenhall, Pratul P. Srinivasan, Rodrigo Ortiz Cayon, Nima Khademi Kalantari, Ravi Ramamoorthi, Ren Ng, and Abhishek Kar. Local light field fusion: practical view synthesis with prescriptive sampling guidelines. *ACM Trans. Graph.*, 2019. 2
- [28] Ben Mildenhall, Pratul P. Srinivasan, Matthew Tancik, Jonathan T. Barron, Ravi Ramamoorthi, and Ren Ng. Nerf:

- Representing scenes as neural radiance fields for view synthesis. In *ECCV*, 2020. 2
- [29] Ben Mildenhall, Pratul P. Srinivasan, Matthew Tancik, Jonathan T. Barron, Ravi Ramamoorthi, and Ren Ng. Nerf: Representing scenes as neural radiance fields for view synthesis. In *European Conference on Computer Vision*, pages 405–421. Springer, 2020. 2, 3
- [30] Thomas Müller, Alex Evans, Christoph Schied, and Alexander Keller. Instant neural graphics primitives with a multiresolution hash encoding. *ACM Trans. Graph.*, 2022. 2
- [31] Thomas Müller, Alex Evans, Christoph Schied, and Alexander Keller. Instant neural graphics primitives with a multiresolution hash encoding. *ACM Transactions on Graphics*, 41(4):1–15, 2022. 2, 3, 4, 5, 6, 7, 1
- [32] Sameera Ramasinghe and Simon Lucey. Beyond periodicity: Towards a unifying framework for activations in coordinate-mlps. In *European Conference on Computer Vision*, pages 142–158. Springer, 2022. 2
- [33] Christian Reiser, Songyou Peng, Yiyi Liao, and Andreas Geiger. Kilonerf: Speeding up neural radiance fields with thousands of tiny mlps. In *Proceedings of the IEEE/CVF International Conference on Computer Vision*, pages 14335–14345, 2021. 1
- [34] Vishwanath Saragadam, Jasper Tan, Guha Balakrishnan, Richard G Baraniuk, and Ashok Veeraraghavan. Miner: Multiscale implicit neural representation. In *European Conference on Computer Vision*, pages 318–333. Springer, 2022. 2
- [35] Vincent Sitzmann, Julien Martel, Alexander Bergman, David Lindell, and Gordon Wetzstein. Implicit neural representations with periodic activation functions. *Advances in Neural Information Processing Systems*, 33:7462–7473, 2020. 2
- [36] Cheng Sun, Min Sun, and Hwann-Tzong Chen. Direct voxel grid optimization: Super-fast convergence for radiance fields reconstruction. In *CVPR*, 2022. 2
- [37] Cheng Sun, Min Sun, and Hwann-Tzong Chen. Direct voxel grid optimization: Super-fast convergence for radiance fields reconstruction. In *Proceedings of the IEEE/CVF Conference on Computer Vision and Pattern Recognition*, pages 5459–5469, 2022. 5
- [38] Towaki Takikawa, Joey Litalien, Kangxue Yin, Karsten Kreis, Charles Loop, Derek Nowrouzezahrai, Alec Jacobson, Morgan McGuire, and Sanja Fidler. Neural geometric level of detail: Real-time rendering with implicit 3d shapes. In *Proceedings of the IEEE/CVF Conference on Computer Vision and Pattern Recognition*, pages 11358–11367, 2021. 2
- [39] Matthew Tancik, Vincent Casser, Xinchen Yan, Sabeek Pradhan, Ben Mildenhall, Pratul P Srinivasan, Jonathan T Barron, and Henrik Kretzschmar. Block-nerf: Scalable large scene neural view synthesis. In *Proceedings of the IEEE/CVF Conference on Computer Vision and Pattern Recognition*, pages 8248–8258, 2022. 1
- [40] Justus Thies, Michael Zollhöfer, and Matthias Nießner. Deferred neural rendering: image synthesis using neural textures. *ACM Trans. Graph.*, 2019. 2
- [41] Haithem Turki, Deva Ramanan, and Mahadev Satyanarayanan. Mega-NerF: Scalable construction of large-scale nerfs for virtual fly-throughs. In *Proceedings of the IEEE/CVF Conference on Computer Vision and Pattern Recognition*, pages 12922–12931, 2022. 1
- [42] Haithem Turki, Michael Zollhöfer, Christian Richardt, and Deva Ramanan. Pynerf: Pyramidal neural radiance fields. *Advances in Neural Information Processing Systems*, 36, 2024. 1
- [43] Michael Waechter, Nils Moehrl, and Michael Goesele. Let there be color! large-scale texturing of 3d reconstructions. In *ECCV*, 2014. 2
- [44] Chen Wang, Xian Wu, Yuan-Chen Guo, Song-Hai Zhang, Yu-Wing Tai, and Shi-Min Hu. NeRF-SR: High quality neural radiance fields using supersampling. In *Proceedings of the ACM International Conference on Multimedia*, pages 6445–6454, 2022. 5
- [45] Peng Wang, Lingjie Liu, Yuan Liu, Christian Theobalt, Taku Komura, and Wenping Wang. NeuS: Learning neural implicit surfaces by volume rendering for multi-view reconstruction. *arXiv preprint arXiv:2106.10689*, 2021. 2
- [46] Peng Wang, Yuan Liu, Zhaoxi Chen, Lingjie Liu, Ziwei Liu, Taku Komura, Christian Theobalt, and Wenping Wang. F2-nerf: Fast neural radiance field training with free camera trajectories. In *Proceedings of the IEEE/CVF Conference on Computer Vision and Pattern Recognition*, pages 4150–4159, 2023. 2
- [47] Suttisak Wizadwongsa, Pakkapon Phongthawee, Jiraphon Yenphraphai, and Supasorn Suwajanakorn. Nex: Real-time view synthesis with neural basis expansion. In *Proceedings of the IEEE/CVF Conference on Computer Vision and Pattern Recognition*, pages 8534–8543, 2021. 3
- [48] Daniel N. Wood, Daniel I. Azuma, Ken Aldinger, Brian Curless, Tom Duchamp, David Salesin, and Werner Stuetzle. Surface light fields for 3d photography. In *SIGGRAPH*, 2000. 2
- [49] Yuanbo Xiangli, Linning Xu, Xingang Pan, Nanxuan Zhao, Anyi Rao, Christian Theobalt, Bo Dai, and Dahua Lin. BungeeNeRF: Progressive neural radiance field for extreme multi-scale scene rendering. In *European Conference on Computer Vision*, pages 106–122. Springer, 2022. 2, 5
- [50] Haolin Xiong, Sairisheek Muttukuru, Rishi Upadhyay, Pradyumna Chari, and Achuta Kadambi. Sparsegs: Real-time 360sparse view synthesis using gaussian splatting, 2024. 2
- [51] Linning Xu, Yuanbo Xiangli, Sida Peng, Xingang Pan, Nanxuan Zhao, Christian Theobalt, Bo Dai, and Dahua Lin. Grid-guided neural radiance fields for large urban scenes. In *Proceedings of the IEEE/CVF Conference on Computer Vision and Pattern Recognition (CVPR)*, pages 8296–8306, 2023. 1
- [52] Lior Yariv, Yoni Kasten, Dror Moran, Meirav Galun, Matan Atzmon, Basri Ronen, and Yaron Lipman. Multiview neural surface reconstruction by disentangling geometry and appearance. *NeurIPS*, 2020. 2
- [53] Alex Yu, Ruilong Li, Matthew Tancik, Hao Li, Ren Ng, and Angjoo Kanazawa. Plenotrees for real-time rendering of neural radiance fields. In *Proceedings of the IEEE/CVF International Conference on Computer Vision*, pages 5752–5761, 2021. 2

- [54] Alex Yu, Sara Fridovich-Keil, Matthew Tancik, Qinhong Chen, Benjamin Recht, and Angjoo Kanazawa. Plenoxels: Radiance fields without neural networks. In *CVPR*, 2022. [2](#)
- [55] Zehao Yu, Anpei Chen, Binbin Huang, Torsten Sattler, and Andreas Geiger. Mip-splatting: Alias-free 3d gaussian splatting. In *Proceedings of the IEEE/CVF Conference on Computer Vision and Pattern Recognition (CVPR)*, pages 19447–19456, 2024. [2](#)
- [56] Kun Zhou, Wenbo Li, Yi Wang, Tao Hu, Nianjuan Jiang, Xiaoguang Han, and Jiangbo Lu. Nerflix: High-quality neural view synthesis by learning a degradation-driven inter-viewpoint mixer. In *Proceedings of the IEEE/CVF Conference on Computer Vision and Pattern Recognition (CVPR)*, pages 12363–12374, 2023. [1](#)
- [57] Zuo-Liang Zhu, Beibei Wang, and Jian Yang. Gs-ror: 3d gaussian splatting for reflective object relighting via sdf priors, 2024. [2](#)

LookCloser: Frequency-aware Radiance Field for Tiny-Detail Scene

Supplementary Material

This supplementary material includes video results for scenes from the Multi-frequency datasets. In the following sections, we first introduce additional implementation details (Sec. 7). Moreover, we provide additional experiments on frequency level evaluation from 2D to 3D on the real dataset Mip-NeRF360-v2 (Sec. 8). Finally, we present more experimental results (Sec. 9).

7. Additional Implementation Details

7.1. Dataset

We captured our dataset using two different cameras. We collected normal-resolution images with a panoramic camera to achieve a more comprehensive 360-degree field of view for better scene structure reconstruction. And high-resolution images were captured with a DSLR (Digital Single-Lens Reflex) camera. To obtain camera poses, we perform Structure from Motion reconstruction for both the panoramic and high-resolution images. We use shared intrinsic between all images of the same camera model in a scene, and calibrate using the OpenCV radial distortion model. We then project the panoramic images into six 600×600 perspective images, each with FOV of 60° to accommodate the perspective camera model commonly used in most NeRF models. We adopt a common dataset splitting method, selecting one out of every eight panoramic/high-resolution images as the test set, with the remainder constituting the training set.

7.2. Architecture details

We adopt a setup similar to Instant-NGP [31], utilizing 16 grid scales with the maximum resolution being $2048 \times \text{scene size}$ and the minimum resolution being 16, employing 2 feature channels per level. In our dataset, due to the larger scene sizes, we set the size of the hash table storing feature vector for each level to 2^{23} to mitigate the impact of hash collisions on scene representation. For other general scenes, we use an identical hash table size of 2^{19} to Instant-NGP [31]. The fetched hash feature vectors are down-weighted before being concatenated and fed to a one-layer MLP with 64 hidden units to get the scene features and the volume densities. Subsequently, the scene features are concatenated with the spherical harmonics encoding of the view directions, which is then input to a subsequent two-layer MLP of width 64 to yield the RGB colors.

7.3. Frequency Grid

To represent the frequency distribution in the 3D space, we maintain a frequency grid with a resolution of $128 \times \text{AABB}$,

where AABB, short for Axis-Aligned Bounding Box, denotes the scene size. For each scene, we adjust the AABB based on the 3D points from the SfM reconstruction to ensure it encompasses the majority of the 3D points. Each grid cell stores the frequency level as a uint8 number.

Initialization. Once we have the 2D frequencies of all training patches, we first calculate the 3D frequency of each 3D point p_i . After that, each 3D point is reprojected to obtain a set of observation patches $\{P_{ij} | j = 1, \dots, n\}$ and derive a set of 3D frequencies $\{f_{3D_{ij}} | j = 1, \dots, n\}$ with the depth of the point. To mitigate the influence of noisy patches, we take the median of this set as the 3D frequency f_{3D_i} for that point. Assuming that the frequencies at each level are $\{f_{3D_\ell} | \ell = 0, \dots, n_\ell\}$, we take the frequency level ℓ_i as $\arg \min_\ell (|f_{3D_\ell} - f_{3D_i}|)$. The frequency grid is then initialized to the maximum of the frequency levels of all 3D points within the grid.

Re-weighting. Unlike Instant-NGP [31], which directly concatenates feature vectors as the input for the tiny MLP, we take into account the 3D frequency at that point and re-weight different frequency components accordingly. Instead, we use the quantified frequency level ℓ as a threshold and apply a down-weighting to frequency components that are higher than ℓ . We compute the down-weighting factor w using an approximation for $\text{erf}(x)$:

$$\text{erf}(x) \approx \text{sign}(x) \sqrt{1 - \exp(-(4/\pi)x^2)} \quad (10)$$

Updating. We update the grids after every 1024 training iterations by the following steps. We first render the depth of the center pixel of a training patch P_i . Then, the 2D frequency of the patch is projected to the corresponding 3D point to obtain its 3D frequency f_{3D_i} and frequency level ℓ_i . Finally, the value ℓ of the frequency grid where the 3D point resides is then updated to $\max(\ell_i, \ell)$.

Frequency-averaged sampling (FAS). We divide the training batch into N segments based on the frequency quantization results. The sampling frequency is evenly distributed within a preset range of $[1, 3]$, meaning that the highest frequency content is sampled with a probability three times that of the lowest frequency. In our experiments, we found that this is a more stable setting compared to directly using the frequency ratio as the sampling proportion.

7.4. Loss Functions

As described in the main paper, the training loss is defined as

$$\mathcal{L}_{total} = \mathcal{L}_{recon}(\hat{\mathbf{c}}, \mathbf{c}_{gt}) + \lambda_{depth} \mathcal{L}_{depth}(\hat{\mathbf{d}}, \mathbf{d}_{gt}) + \lambda_{dist} \mathcal{L}_{dist}(\mathbf{s}_d, \mathbf{w}), \quad (11)$$

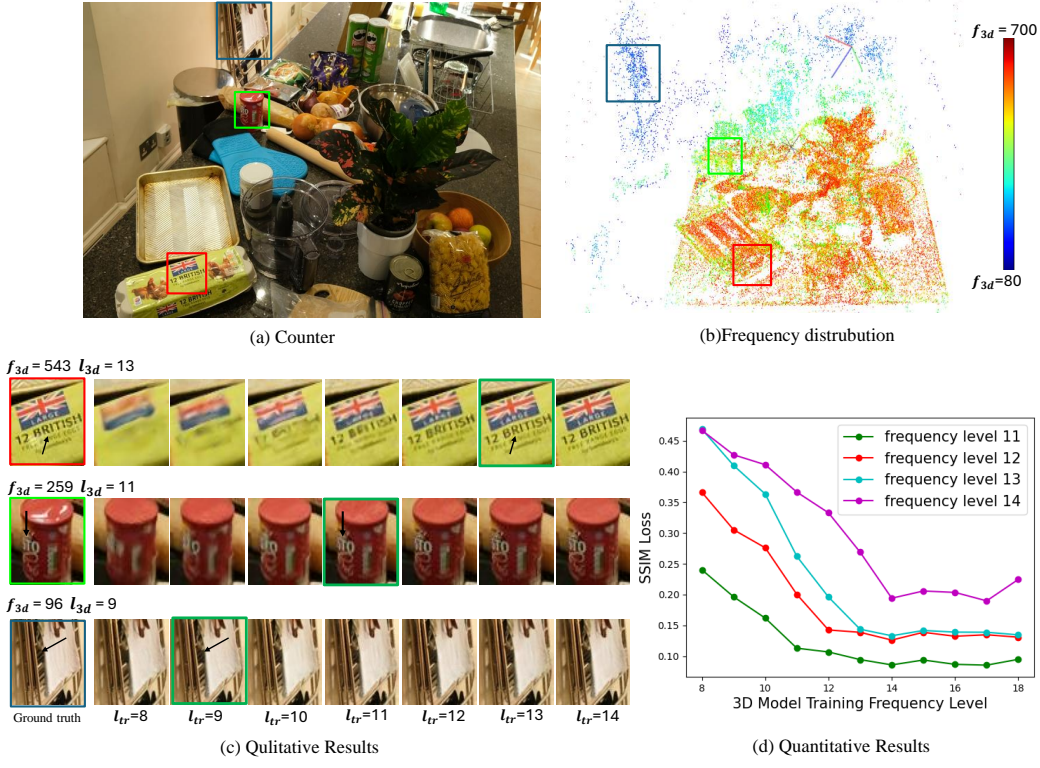


Figure 7. We test the effectiveness of frequency quantification on the real dataset NeRF-360-v2. (a) is a ground truth image from the *counter* dataset. (b) is the colored point cloud after the 3D frequency initialization of all 3D points, where colors leaning towards blue indicate lower frequencies and those towards red indicate higher frequencies. It can be observed that there is a trend of higher frequencies with smaller depths. Moreover, different regions at the same depth also exhibit varying distributions of 3D frequencies. In (a), we selected three patches with different frequency levels ℓ_{3D} 9, 11, and 13, represented by blue, green, and red, respectively. (c) is the rendering results of these three patches at training frequency level ℓ_{tr} ranging from 8 to 14. It can be noticed that details are not well recovered when ℓ_{tr} is lower than the quantified ℓ_{3D} , and when ℓ_{tr} exceeds ℓ_{3D} , there is no significant improvement in the quality of the rendering images. (d) shows the distribution of average SSIM Loss for patches of different frequency levels in the *counter* dataset at various training frequency levels ℓ_{tr} . Once ℓ_{tr} reaches the quantified ℓ_{3D} , there is no significant decrease in loss.

where the first term $\mathcal{L}_{recon}(\hat{\mathbf{c}}, \mathbf{c}_{gt}) = \sqrt{(\hat{\mathbf{c}} - \mathbf{c}_{gt})^2 + \epsilon}$ is a color reconstruction loss [2], $\hat{\mathbf{c}}$ is the rendered pixel color, \mathbf{c}_{gt} is the ground-truth pixel color, and $\epsilon = 10^{-4}$, and the last term is the regularization loss.

The depth loss \mathcal{L}_{depth} of the sampled ray is defined by

$$\mathcal{L}_{depth}(\hat{\mathbf{d}}, \mathbf{d}_{gt}) = \sqrt{(\hat{\mathbf{d}} - \mathbf{d}_{gt})^2 + \epsilon} \quad (12)$$

where the depth of a ray is computed by the weighted sum of the sampled distance that $d = \sum_i w_i t_i$, and $\{w_i\}$ are the weights computed by the volume rendering. We only use the depth loss in early training for pixels with GT depth from the sparse point cloud to avoid incorrect geometry structure.

The regularization loss is proposed by Mip-NeRF360 [2]. We use it to prevent floaters and background collapse, which is defined as

$$\mathcal{L}_{dist}(\mathbf{s}_d, \mathbf{w}) = \sum_{i,j} w_i w_j \left| \frac{s_i + s_{i+1}}{2} - \frac{s_j + s_{j+1}}{2} \right| + \frac{1}{3} \sum_i w_i^2 (s_{i+1} - s_i), \quad (13)$$

where \mathbf{s}_d is the set of normalized ray distances and \mathbf{w} is the set of weights. It penalizes the discreteness to encourage the formation of thinner surfaces. In contrast to Mip-NeRF360 using a proposal network to obtain sampling suggestions, we compute this discrete version of sampling distribution regularization along the entire ray.

The hyperparameters λ_{dist} , λ_{depth} are used to balance the data terms and the regularize; we set $\lambda_{dist} = 0.01$, $\lambda_{depth} = 0.001$ for all experiments.



Figure 8. Qualitative comparisons with the Instant-NGP [31] that has a larger hash table size (Big) on the Mip-NeRF360-v2 [2] and Tank and Temples [19] dataset.

Method	room	counter	kitchen	bonsai	average
TensoRF	0.791	0.697	0.560	0.783	0.708
INGP-Base	0.893	0.845	0.857	0.924	0.879
INGP-Big	0.900	0.868	0.907	0.922	0.900
Mip-NeRF360	0.913	0.895	0.920	0.939	0.916
3D-GS	0.914	0.905	0.922	0.938	0.919
Ours	0.936	0.908	0.931	0.946	0.931

Table 4. SSIM on the Mip-NeRF360-v2 dataset

Method	room	counter	kitchen	bonsai	average
TensoRF	0.419	0.469	0.516	0.389	0.448
INGP-Base	0.242	0.255	0.170	0.198	0.216
INGP-Big	0.254	0.256	0.158	0.209	0.219
Mip-NeRF360	0.211	0.203	0.126	0.177	0.179
3D-GS	0.220	0.204	0.129	0.205	0.189
Ours	0.191	0.184	0.123	0.159	0.165

Table 5. LPIPS on the Mip-NeRF360-v2 dataset

8. Evaluate Frequency Level from 2D to 3D

In this section, we further demonstrate the effectiveness of frequency quantification from 2D to 3D using the real dataset Mip-NeRF360-v2.

Visualization of Frequency Distribution. As described in the main paper, we reproject each 3D point from the sparse point cloud back into all the observation images. Then we calculate the 3D frequency set S based on all the corresponding patches. The median of S is taken as the 3D frequency for that point. Fig. 7(b) shows a visualization of the 3D frequency distribution of all 3D points after initialization for the dataset *counter* in Mip-NeRF360-v2, where the color of the points indicates the corresponding 3D frequency, with points closer to blue indicating a lower frequency and those closer to red indicating a higher frequency. Fig. 7(a) represents the ground truth image, where the blue, green, and red boxes represent three patches with 3D frequencies from low to high as shown in Fig. 7(b).

Qualitative Results. Fig. 7(c) depicts the visual comparison of the rendering results under varying training frequencies of the three patches mentioned above, where the boxed patches represent the rendering results under the quantified

Method	room	counter	kitchen	bonsai	average
TensoRF	26.88	23.39	23.12	25.46	24.71
INGP-Base	30.31	26.21	29.00	31.08	29.15
INGP-Big	30.19	27.27	30.86	30.57	29.72
Mip-NeRF360	31.40	29.44	32.02	33.11	31.49
3D-GS	30.63	28.70	30.32	31.98	30.95
Ours	31.45	29.19	31.41	32.75	31.20

Table 6. PSNR on the Mip-NeRF360-v2 dataset

3D frequency level ℓ_{3D} . It is clearly demonstrated that when the training frequency level is lower than ℓ_{3D} , the network is unable to fully recover the detailed information. Conversely, when the training frequency exceeds the quantified 3D frequency, the network does not yield better results either.

Quantitative Results. Furthermore, in Fig. 7(d), the lines in green, red, blue, and purple correspond to patches with 3D frequency levels of 11, 12, 13, and 14, respectively. With the escalation of the training frequency from 8 to 14, there is a progressive reduction in the SSIM loss for the generated patches. Upon reaching the quantified 3D frequency for each patch with the training frequency, the SSIM loss reduction becomes more consistent. This observation suggests two key points: firstly, the necessary minimum NeRF frequency level for the complete reconstruction of the scene’s diverse 3D frequency structures and textures is variable; secondly, the 3D frequency estimation we employ for the content provides an accurate reflection of their actual frequencies.

9. More Experimental Details

9.1. Quantitative Results on Standard Datasets

We compare our methods against our baselines on the standard datasets whose scenes have a smaller frequency span and size. The quantitative results are shown in the Tab. 2. Here we show the qualitative comparisons with the Instant-NGP [31], as depicted in Fig. 8. Our methods render sharper and clearer high-frequency contents than the Instant-NGP, indicating that while our frequency-aware framework is designed to handle high-quality model scene structures and details in scenarios with significant frequency disparities, it still generalizes well on standard datasets, enhancing rendering quality, particularly in high-frequency details.

9.2. More Ablation Studies

Component Ablation. We conducted ablation experiments in each scene, and the results are shown in Tab. 7. The results indicate that the impact of different features on overall performance varies across scenes of different scales. In particular, in high-frequency scenes captured at close range, such as the “Flower Shop”, the sampling interval adjustment has a more pronounced effect. This tendency is par-

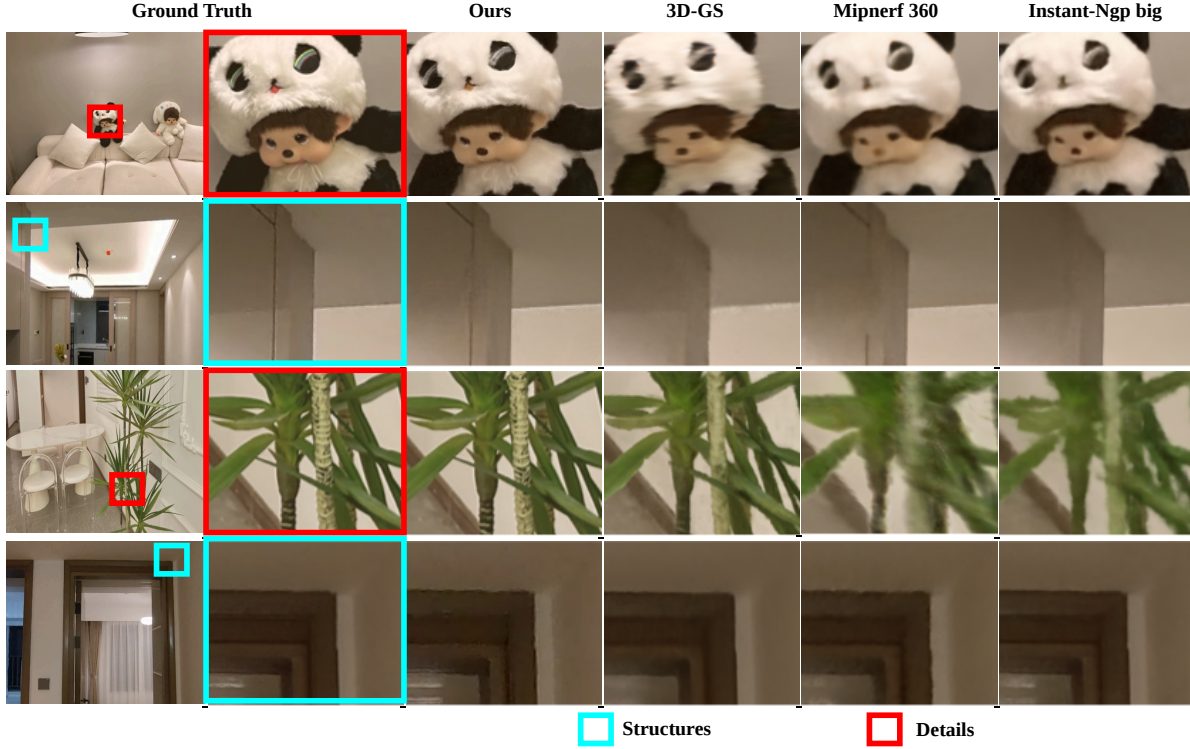


Figure 9. Additional visual comparisons on the Multi-frequency dataset.

Setting	FlowerShop	Home	DollsRoom	MusicRoom	PlantRoom	Average
normal-res(600×600)						
w/o Feature Re-weighting	28.19	32.93	34.12	33.46	33.42	32.42
w/o FAS	26.36	32.93	34.18	33.50	33.59	32.11
w/o Interval Adjustment	27.12	32.62	34.09	32.30	32.96	31.82
Our Complete Model	28.23	32.91	34.20	33.52	33.36	32.44
high-res(4032×3024)						
w/o Feature Re-weighting	24.62	26.14	28.41	26.54	24.55	26.05
w/o FAS	24.01	26.47	28.74	26.84	23.98	25.97
w/o Interval Adjustment	23.82	25.79	28.31	26.02	23.81	25.55
Our Complete Model	24.86	26.24	28.75	26.97	24.63	26.29

Table 7. Ablation Studies on Multi-frequency dataset

ticularly evident in large-scale datasets or close-range captures. As shown in Figure. 10, close-range high-frequency content becomes blurred in the absence of sampling interval adjustment, which aligns with the description in Section 4.2 of the paper. Due to variations in the proportion of high-frequency data within scenes, the efficacy of FAS also varies. Balancing training batches sometimes enhances high-frequency effects, while at other times it may diminish them, depending on the distribution of scene data. Feature re-weighting enhances the network’s efficiency in utilizing various frequency ranges, particularly when there is abundant scene content and limited network capacity.

9.3. Per-Scene Metrics

We provide the per-scene results on the Multi-frequency dataset, Tanks&Temples dataset, and Mip-NeRF360-v2 dataset in Tab. 14 - 5. The results are reported in the metrics of PSNR, SSIM, and LPIPS. We provide more visual comparisons on the Multi-frequency dataset in Fig. 9.

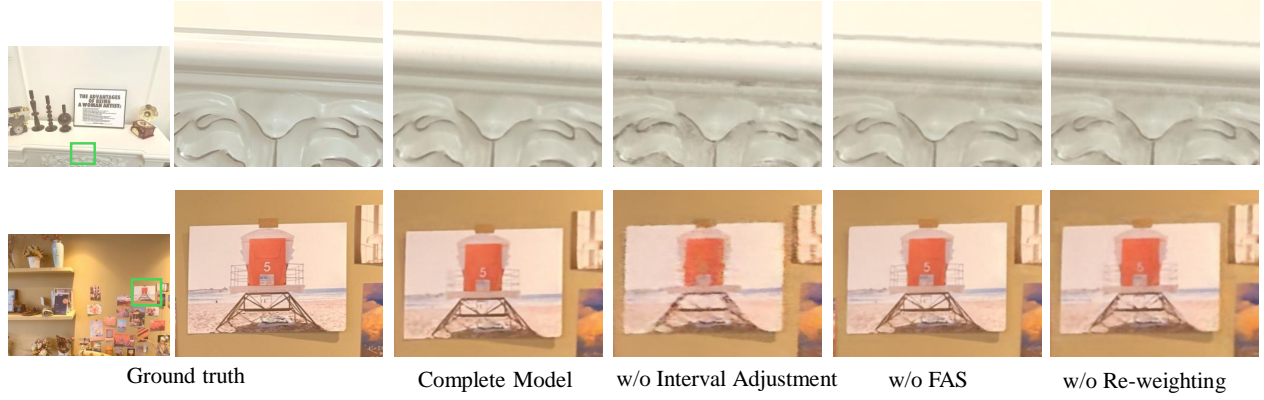


Figure 10. Additional visual comparisons with different settings of our method.

Table 8. PSNR on the Multi-frequency dataset(structure view)

PSNR	FlowerShop	Home	DollsRoom	MusicRoom	PlantRoom	Average
TensorRF	24.36	29.63	30.78	30.69	28.94	28.88
INGP-Base	25.31	30.10	32.07	31.78	32.07	30.27
INGP-Big	26.22	30.94	32.75	32.25	32.67	30.97
Mip-NeRF360	26.90	32.01	31.28	32.59	31.15	30.79
3D-GS	27.02	32.08	31.30	32.74	31.17	30.85
Ours	28.23	32.91	34.2	33.52	33.36	32.44

Table 9. SSIM on the Multi-frequency dataset(structure view)

SSIM	FlowerShop	Home	DollsRoom	MusicRoom	PlantRoom	Average
TensorRF	0.740	0.884	0.893	0.890	0.862	0.854
INGP-Base	0.791	0.902	0.925	0.921	0.924	0.893
INGP-Big	0.830	0.918	0.934	0.930	0.933	0.909
Mip-NeRF360	0.851	0.935	0.903	0.923	0.896	0.906
3D-GS	0.846	0.931	0.900	0.910	0.899	0.897
Ours	0.890	0.942	0.946	0.931	0.937	0.929

Table 10. LPIPS on the Multi-frequency dataset(structure view)

LPIPS	FlowerShop	Home	DollsRoom	MusicRoom	PlantRoom	Average
TensorRF	0.310	0.230	0.233	0.240	0.266	0.256
INGP-Base	0.267	0.205	0.206	0.207	0.196	0.216
INGP-Big	0.210	0.169	0.181	0.184	0.172	0.183
Mip-NeRF360	0.181	0.158	0.208	0.187	0.206	0.188
3D-GS	0.177	0.164	0.217	0.189	0.211	0.191
Ours	0.148	0.130	0.146	0.162	0.152	0.148

Table 11. PSNR on the Multi-frequency dataset(detail view)

PSNR	FlowerShop	Home	DollsRoom	MusicRoom	PlantRoom	Average
TensorRF	23.23	16.54	26.93	25.19	21.91	22.76
INGP-Base	22.27	22.82	26.75	24.49	21.83	23.63
INGP-Big	22.65	23.36	27.02	24.90	22.06	24.00
Mip-NeRF360	23.27	24.28	25.98	25.28	21.97	24.16
3D-GS	23.42	24.46	26.11	25.41	22.01	24.29
Ours	24.86	26.24	28.75	26.97	24.64	26.29

Table 12. SSIM on the Multi-frequency dataset(detail view)

SSIM	FlowerShop	Home	DollsRoom	MusicRoom	PlantRoom	Average
TensoRF	0.726	0.655	0.791	0.882	0.852	0.781
INGP-Base	0.716	0.717	0.769	0.868	0.848	0.784
INGP-Big	0.720	0.722	0.770	0.870	0.849	0.786
Mip-NeRF360	0.686	0.731	0.795	0.884	0.863	0.792
3D-GS	0.735	0.758	0.791	0.893	0.833	0.802
Ours	0.770	0.813	0.817	0.924	0.892	0.843

Table 13. LPIPS on the Multi-frequency dataset(detail view)

LPIPS	FlowerShop	Home	DollsRoom	MusicRoom	PlantRoom	Average
TensoRF	0.459	0.592	0.415	0.316	0.367	0.430
INGP-Base	0.466	0.500	0.404	0.323	0.346	0.408
INGP-Big	0.485	0.449	0.401	0.316	0.337	0.398
Mip-NeRF360	0.421	0.459	0.413	0.292	0.343	0.383
3D-GS	0.422	0.454	0.423	0.306	0.347	0.390
Ours	0.384	0.361	0.367	0.250	0.302	0.332

Table 14. Results on the Tanks&Temples dataset

Dataset	Train			Truck			Average		
Method—Metric	PSNR [↑]	SSIM [↑]	LPIPS _(VGG) [↓]	PSNR [↑]	SSIM [↑]	LPIPS _(VGG) [↓]	PSNR [↑]	SSIM [↑]	LPIPS _(VGG) [↓]
TensoRF	18.73	0.569	0.490	20.30	0.657	0.411	19.52	0.613	0.451
INGP-Base	20.43	0.684	0.367	22.69	0.777	0.269	21.56	0.731	0.318
INGP-Big	20.39	0.711	0.332	22.98	0.803	0.227	21.69	0.757	0.280
Mip-NeRF360	19.52	0.660	0.354	24.91	0.857	0.159	22.22	0.759	0.257
3D-GS	23.06	0.813	0.200	25.66	0.849	0.226	24.36	0.831	0.213
Ours	23.13	0.802	0.197	25.77	0.841	0.210	24.45	0.821	0.205

Table 15. Quantitative comparisons

	Structure View(600×600)			Detail View(4032× 3024)		
Method(Mem)	PSNR [↑]	SSIM [↑]	LPIPS [↓]	PSNR [↑]	SSIM [↑]	LPIPS [↓]
BungeeNeRF	22.21	0.524	0.428	19.41	0.401	0.587
BungeeNeRF(adapted)	30.42	0.903	0.194	24.07	0.770	0.379
Mip-NeRF360	30.79	0.906	0.188	24.16	0.792	0.383
Ours	32.44	0.929	0.148	26.29	0.843	0.332